

FAST DATA INVERSION FOR HIGH-DIMENSIONAL DYNAMICAL SYSTEMS FROM NOISY MEASUREMENTS

BY YIZI LIN^{*1,a}, XUBO LIU^{1,b} PAUL SEGALL^{2,d} AND MENGYANG GU^{1,c}

¹*Department of Statistics and Applied Probability, University of California, Santa Barbara*
^a*lin768@umail.ucsb.edu*; ^b*xubo@umail.ucsb.edu*; ^c*mengyang@pstat.ucsb.edu*

²*Department of Geophysics, Stanford University*
^d*segall@stanford.edu*

In this work, we develop a scalable approach for a flexible latent factor model for high-dimensional dynamical systems. Each latent factor process has its own correlation and variance parameters, and the orthogonal factor loading matrix can be either fixed or estimated. We utilize an orthogonal factor loading matrix that avoids computing the inversion of the posterior covariance matrix at each time of the Kalman filter, and derive closed-form expressions in an expectation-maximization algorithm for parameter estimation, which substantially reduces the computational complexity without approximation. Our study is motivated by inversely estimating slow slip events from geodetic data, such as continuous GPS measurements. Extensive simulated studies illustrate higher accuracy and scalability of our approach compared to alternatives. By applying our method to geodetic measurements in the Cascadia region, our estimated slip better agrees with independently measured seismic data of tremor events. The substantial acceleration from our method enables the use of massive noisy data for geological hazard quantification and other applications.

1. Introduction. Latent factor models of time-dependent data have wide applications, including modeling multiple time series in economics (Lam and Yao, 2012) and estimating unobservable geophysical processes by ground deformation measurements (Segall and Matthews, 1997). Though applications differ, the latent factor model can be broadly classified into two categories with either fixed or data-dependent factor loading matrices.

Basis functions, such as discrete Fourier basis and Green functions, are widely used for inverse estimation of experimental or field observations. Differential dynamic microscopy (Cerbino and Trappe, 2008), for instance, is a physical approach for estimating the rheological properties of the materials by microscopy videos. The estimation corresponds to minimizing the temporal autocorrelation in the Fourier space by a latent factor model with the complex conjugate of the discrete Fourier basis (Gu et al., 2024a). Green's functions, as another example, relate field observations to unobserved displacement at different spatial scales, such as cellular force estimation by traction force microscopy (Sabass et al., 2008) and slip estimation by geodetic data (Yabuki and Matsu'Ura, 1992).

On the other hand, the factor loading matrix can be estimated by data. Probabilistic models were built to understand the underlying model assumptions made by these estimations. The loading matrix estimated by the principal component analysis (Berkooz et al., 1993), for instance, is shown to be the maximum marginal likelihood estimator of a latent factor model with random factors independently distributed as standard Gaussian distributions (Tipping and Bishop, 1999). Various approaches extend the independent assumption for correlated

*The first two authors contribute equally. Correspondence should be addressed to Mengyang Gu.

Keywords and phrases: Bayesian prior, latent factor models, Gaussian processes, expectation-maximization algorithm, Kalman filter.

data. For instance, dynamic mode decomposition is a popular approach of linearizing the one-step-ahead transition operator of nonlinear dynamical systems and reconstructing the dynamics by eigenpairs of the linear mapping matrix (Schmid, 2010; Tu et al., 2014). In Gu et al. (2024b), the authors show the estimation of the dynamic mode decomposition is equivalent to the maximum likelihood estimator of the linear mapping matrix in a vector autoregressive model of noise-free observations. As another example, each latent factor is modeled by a Gaussian process in coregionalization models (Gelfand et al., 2004).

In this work, we develop a scalable and efficient approach for latent factor models with correlated factors and an orthogonal factor loading matrix either fixed or estimated by data. Our contributions are threefold. First, estimating a large number of correlation parameters in multivariate Gaussian processes is a fundamental challenge. When each latent factor process has distinct parameters, conventional strategies, such as posterior sampling or numerical optimization can be prohibitively slow for estimating a large number of parameters. We developed a new expectation-maximization (EM) algorithm. We surprisingly found that the estimation of the factor loading matrix, correlation and variance parameters, all have a closed-form expression in the algorithm. In particular, the correlation parameters of latent processes can be solved by cubic equations of order three. Furthermore, we construct an orthogonal latent factor loading matrix which enables us to filter each projected latent factor process separately without approximation, thereby avoiding large matrix inversion conventionally needed at each time in the Kalman filter (Kalman, 1960). Second, we model latent factors by a multivariate Ornstein-Uhlenbeck process that contains distinct correlation and variance parameters. Our model extends the probabilistic model of the dynamic mode decomposition by including the noise model and utilizing a symmetric factor loading matrix for reducing the space in estimation. Third, we developed a new way to estimate the number of factors with either fixed or estimated factor loading matrix by matching the estimated noise variance with its measurement. Our study is motivated by fault slip estimation from geodetic measurements, but the new approach has broad applications for problems in science and engineering.

1.1. Motivating example: Fault slip estimation by geodetic data. Ground deformation observations, such as continuous Global Positioning System (GPS) observations (Segall and Matthews, 1997) and interferometric synthetic-aperture radar interferograms (Anderson et al., 2019), have been widely used to quantify geological hazards, including volcanic eruptions and earthquakes. The goal of our application is to estimate fault slip that quantifies the relative movement velocities of two sides of the faults (Bürgmann, 2018). Since slip cannot be directly observed, time-dependent ground deformation information from GPS data has been used for slip estimation (Bock et al., 1993).

The Cascadia subduction zone is known to experience aseismic, transient slip events known as Slow Slip Events (Gomberg et al., 2010). Slow slip events, recorded by high precision GPS data, have been found to be spatially and temporally associated with ‘tectonic tremor’, composed of low-frequency earthquakes recorded on seismic stations. We utilized the GPS data in the Cascadia subduction zone, publicly available at the Plate Boundary Observatory, for estimating the slip on the megathrust fault from June 2011 to August 2011 (Bartlow et al., 2011). Denote the p_y -dimensional observations $\mathbf{y}(\mathbf{x}, t) \in \mathbb{R}^{p_y}$ at location $\mathbf{x} \in \mathbb{R}^{p_x}$ and time $t \in \mathbb{R}$. In our application, as the vertical displacement measurements contain little information for slip migration, the ground displacement measurement $\mathbf{y}(\mathbf{x}, t)$ is a two-dimensional vector in the East-West and North-South directions observed at equally spaced time t at a GPS station, with spatial coordinates $\mathbf{x} = (x_1, x_2)$, and hence $p_x = p_y = 2$. The network inversion filter introduced in Segall and Matthews (1997) is a popular approach for modeling the displacement at the Earth’s surface by: $\mathbf{y}(\mathbf{x}, t) = \int \mathbf{G}(\mathbf{x}, \boldsymbol{\xi}) \mathbf{z}_s(\boldsymbol{\xi}, t) d\boldsymbol{\xi} + \boldsymbol{\mu}(\mathbf{x}, t) + \boldsymbol{\epsilon}(t)$, where $\mathbf{G}(\mathbf{x}, \boldsymbol{\xi})$ is a quasi-static elastic Green’s function (Aki, 1980) that relates the observations to the unobservable slip $\mathbf{z}_s(\boldsymbol{\xi}, t)$, and $\boldsymbol{\mu}(\mathbf{x}, t)$, the

local benchmark motion, captures the site-specific local motion of the GPS antenna. For data measured over a short period, such as the transient deformations from 2011 in the Cascadia subduction zone considered in this work, the impact of local motion is negligible, and hence we let $\boldsymbol{\mu}(\mathbf{x}, t) = \mathbf{0}$. Furthermore, the reference frame motion is often integrated into this equation by augmented latent processes. The Gaussian noise of the measurement is denoted by $\boldsymbol{\epsilon}(t)$ and the variance of the noise is typically available *a priori* from the GPS measurements.

Suppose we collect GPS observations at \tilde{k} locations, resulting in a $k = p_y \tilde{k}$ vector of observations $\mathbf{y}(t) = [\mathbf{y}(\mathbf{x}_1, t), \mathbf{y}(\mathbf{x}_2, t), \dots, \mathbf{y}(\mathbf{x}_{\tilde{k}}, t)]^T$. In [Segall and Matthews \(1997\)](#), the output vector is modeled below:

$$(1) \quad \mathbf{y}(t) = \mathbf{G}\mathbf{z}_s(t) + \boldsymbol{\epsilon}(t),$$

where \mathbf{G} is a $k \times k'$ matrix of discretized Green's function, $\mathbf{z}_s(t) = [z_s(\boldsymbol{\xi}_1, t), \dots, z_s(\boldsymbol{\xi}_{k'}, t)]^T$ is a k' -vector of unobservable fault slip, with subscript 's' meaning the slip, and the Gaussian noises follow $\boldsymbol{\epsilon}(t) \sim \mathcal{MN}(\mathbf{0}, \sigma_0^2 \mathbf{I}_k)$ with variance σ_0^2 . The (i, h) block of \mathbf{G} is $\mathbf{G}_{i,h} = \mathbf{G}(\mathbf{x}_i, \boldsymbol{\xi}_h) \Delta$ and Δ is the area size in discretization, for $i = 1, \dots, \tilde{k}$ and $h = 1, \dots, k'$ with $\tilde{k} = 100$ GPS stations and $k' = 1978$ discretization points used in estimating the slip propagation in Cascadia ([Bartlow et al., 2011](#)). We found that increasing the number of discretization points has almost no impact on estimates of the slip.

Let \mathbf{U}_0 be $k \times d$ left singular vector matrix corresponding to the largest d singular values in the singular value decomposition (SVD) of the Green's function $\mathbf{G} \approx \mathbf{U}_0 \mathbf{D}_0 \mathbf{V}_0^T$, where \mathbf{D}_0 is a $d \times d$ diagonal matrix and \mathbf{V}_0 is a $k' \times d$ matrix of d right singular vectors. As the number of discretization points k' can be large, the latent slip vector is modeled by a linear combination of the latent processes ([Segall and Matthews, 1997](#)):

$$(2) \quad \mathbf{z}_s(t) = \mathbf{G}^T \mathbf{U}_0 \tilde{\mathbf{z}}(t),$$

with $\tilde{\mathbf{z}}(t)$ being a d -vector of latent processes. The latent process $\tilde{z}_l(t)$ is assumed to follow an integrated Brownian motion in [Segall and Matthews \(1997\)](#). The Kalman filter is used for computing the posterior distribution of the latent process $\tilde{\mathbf{z}}(\cdot)$ and slip estimation. There are several restrictions in this approach. First, the latent process $\tilde{z}_l(\cdot)$ has the same covariance across $l = 1, \dots, d$, yet the random latent factors can have different correlation length scales. Second, one needs to invert a $k \times k$ covariance matrix at each time in the Kalman filter, which is prohibitively slow when the number of GPS stations is moderately large. Third, selecting the number of latent factors is not discussed in this approach.

The goal of this work is to develop a generally applicable approach and scalable algorithm for latent models for estimating the mean of the data and the posterior distribution of the latent variables. For estimating the slip rates in Cascadia between June and August in 2011, we found that the estimated slips had higher spatial correlation with independently detected tremor events not used in estimation. Furthermore, our method is 300 – 3000 times faster than the current method in our real application. The high scalability of our method enables abundant data from GPS networks to be jointly used for hazard quantification.

The rest of the paper is organized as follows. In [Section 2](#), we introduce a flexible latent factor model for high-dimensional dynamical systems with a fast EM algorithm for estimation. We show our model substantially accelerates the computation compared to other approaches in [Section 3](#). Extensive experiments in [Section 4](#) show high accuracy and computational scalability of our approach. In [Section 5](#), we compare our approach with existing ways to estimate the slip migration in the Cascadia region by the GPS data and demonstrate the higher detection rate of tremor events from the independent source of seismic data not used in estimation. We conclude our study and outline future directions in [Section 6](#).

2. Fast and efficient estimation of high-dimensional dynamical systems.

2.1. *A multivariate Ornstein-Uhlenbeck process with an orthogonal basis matrix.* We first introduce our model and its properties. The derivations in this subsection are provided in Section S1 in the supplementary materials. We follow the assumption in (2), which indicates that the mean in (1) is approximated by $\mathbf{G}\mathbf{z}_s(t) \approx \mathbf{U}_0\mathbf{z}(t)$, where $\mathbf{z}(t) = \mathbf{D}_0^2\tilde{\mathbf{z}}(t)$ with the l th entry being $z_l(t)$, and there is no approximation when $k = d$. We model the d -dimensional latent factor process $\mathbf{z}(\cdot)$ by independent Ornstein-Uhlenbeck processes, where each process has its own correlation and variance parameters. Putting together, Equations (1)-(2) lead to

$$(3) \quad \mathbf{y}(t) = \mathbf{U}_0\mathbf{z}(t) + \boldsymbol{\epsilon}(t),$$

$$(4) \quad z_l(t) = \rho_l z_l(t-1) + w_l(t),$$

where \mathbf{U}_0 is a $k \times d$ orthogonal factor loading matrix, either fixed or estimated, which relates the d -dimensional latent factors to k -dimensional measurements. Here, the parameter ρ_l controls the temporal correlation length of the l th latent process, and $w_l(t) \sim \mathcal{N}(0, \sigma_l^2)$ represents the innovation of the l th latent process for $t = 2, \dots, n$, with the initial state being $z_l(1) \sim \mathcal{N}(0, \tau_l^2)$ for $l = 1, \dots, d$. We postpone the discussion of estimating d in Section 2.3. Note that the matrix \mathbf{G} in Equation (1) is typically neither symmetric nor orthogonal, whereas \mathbf{U}_0 is an orthogonal matrix, which brings substantial computational advantages, as will be elaborated soon. In this work, we discuss algorithms for both fixed and estimated \mathbf{U}_0 , which are broadly applicable to many applications. Furthermore, we assume the mean to be zero for simplicity, though additional mean structures can be included in the model.

Lemma 2.1 below connects model in (3)-(4) to the continuous-time multivariate Ornstein-Uhlenbeck process (Gardiner, 1985; Meucci, 2009) with an orthogonal basis matrix.

LEMMA 2.1. *Denote the mean of the k -dimensional processes in (3) by $\mathbf{m}(t) = \mathbf{U}_0\mathbf{z}(t)$. When $\rho \in (0, 1)$, the mean process $\mathbf{m}(t)$ is a discretized process of the continuous-time multivariate Ornstein-Uhlenbeck process, defined by the stochastic differential equation:*

$$(5) \quad d\mathbf{m}(t) = -\mathbf{U}_0\mathbf{D}\mathbf{U}_0^T\mathbf{m}(t)dt + \mathbf{U}_0\tilde{\mathbf{D}}d\mathbf{B}_t,$$

where $\mathbf{D} = \text{diag}(-\log(\rho_1), \dots, -\log(\rho_d))$, $\tilde{\mathbf{D}}$ is a diagonal matrix with the l th element being $\sqrt{\frac{-2\sigma_l^2 \log(\rho_l)}{1-\rho_l^2}}$ for $l = 1, \dots, d$, and \mathbf{B}_t is a vector of independent Brownian motions.

We study the model in (3)-(4) because of its flexibility due to distinct parameters (ρ_l, σ_l^2) for each latent factor l , for $l = 1, \dots, d$ and the computational scalability when the number of latent factors, d , is large. The latent process $z_l(\cdot)$ can be either stationary or nonstationary, depending on the assumption of the initial state, stated in the Lemma 2.2 below.

LEMMA 2.2. *For $l = 1, \dots, d$, the covariance of the process $z_l(\cdot)$ in Equation (4) follows*

$$(6) \quad \text{Cov}[z_l(t), z_l(t')] = \rho_l^{t'-t} \left\{ \rho_l^{2(t-1)} \tau_l^2 + \frac{1 - \rho_l^{2(t-1)}}{(1 - \rho_l^2)} \sigma_l^2 \right\}, \quad \text{for } t' \geq t.$$

In particular, when the variance of initial state is $\tau_l^2 = \frac{\sigma_l^2}{(1-\rho_l^2)}$, $z_l(\cdot)$ is stationary with

$$(7) \quad \text{Cov}[z_l(t), z_l(t')] = \frac{\sigma_l^2}{1 - \rho_l^2} \rho_l^{|t-t'|}.$$

In the rest of the article, we assume that each latent process is stationary by letting $\tau_l^2 = \frac{\sigma_l^2}{1-\rho_l^2}$. Lemma 2.3 outlines key properties of the covariance and precision matrices, which enable us to modify Kalman filter (KF) (Kalman, 1960) and Rauch–Tung–Striebel (RTS) smoother (Rauch et al., 1965) to compute several key quantities in our fast algorithm.

LEMMA 2.3. Assume $\tau_l^2 = \frac{\sigma_l^2}{1-\rho_l^2}$ and denote $\Sigma_l = \frac{\sigma_l^2}{(1-\rho_l^2)}\mathbf{R}_l$ as the covariance matrix of $\mathbf{z}_l = (z_l(1), \dots, z_l(n))^T$ defined in Equation (4). The (t, t') entry of \mathbf{R}_l is $\rho_l^{|t-t'|}$, for $t, t' = 1, 2, \dots, n$. The inverse of \mathbf{R}_l has a tri-diagonal structure, with diagonal entries of $\frac{1}{1-\rho_l^2}$ at the first and last positions, and $\frac{1+\rho_l^2}{1-\rho_l^2}$ at the remaining positions. The primary off-diagonal entries are $-\frac{\rho_l}{1-\rho_l^2}$. Additionally, the determinant of Σ_l follows $|\Sigma_l| = \frac{\sigma_l^{2n}}{1-\rho_l^2}$.

2.2. A fast EM algorithm with closed-form expressions. In this section, we derive a fast EM algorithm for a general scenario where the parameters are $\Theta = (\mathbf{U}_0, \sigma_0^2, \boldsymbol{\rho}, \boldsymbol{\sigma}^2)$ with $\boldsymbol{\rho} = (\rho_1, \rho_2, \dots, \rho_d)$ and $\boldsymbol{\sigma}^2 = (\sigma_1^2, \sigma_2^2, \dots, \sigma_d^2)$. The algorithm leverages KF and RTS smoother for computing required quantities with orthogonal projection, to bypass costly matrix inversion, conventionally required in each step of the KF. A short review of the KF and RTS smoother is provided in Section S2 and the proofs in this subsection are given in Section S3 in the supplementary materials. We call this approach a Fast algorithm of Multivariate Ornstein-Uhlenbeck processes (FMOU).

Let $\mathbf{Y} = [\mathbf{y}(1), \dots, \mathbf{y}(n)]$ represent a $k \times n$ observation matrix and $\mathbf{Z} = [\mathbf{z}_1, \mathbf{z}_2, \dots, \mathbf{z}_d]^T$ denotes a $d \times n$ latent factor matrix. After integrating out the latent factors, the parameters Θ are estimated by the maximum marginal likelihood estimator (MMLE):

$$(8) \quad \Theta^{\text{MMLE}} = \underset{\Theta}{\operatorname{argmax}} \int p(\mathbf{Y} | \mathbf{Z}, \Theta) p(\mathbf{Z} | \Theta) d\mathbf{Z}.$$

Direct optimization of the marginal likelihood of the model in Equations (3) and (4) can be unstable due to optimizing the latent factor matrix in the Stiefel manifold in each step of the optimization (Wen and Yin, 2013) and numerical optimization in high-dimensional parameter space. We develop an EM algorithm which has closed-form expressions in each iteration.

First, the natural logarithm of the joint likelihood of $(\mathbf{Y}, \mathbf{Z} | \Theta)$ follows

$$(9) \quad \ell(\Theta) = C - \frac{nk}{2} \log(\sigma_0^2) - \frac{\operatorname{tr}(\mathbf{Y}^T \mathbf{Y} - 2\mathbf{Y}^T \mathbf{U}_0 \mathbf{Z})}{2\sigma_0^2} - \sum_{l=1}^d \left(\frac{\mathbf{z}_l^T \mathbf{z}_l}{2\sigma_0^2} + \frac{\log |\Sigma_l| + \mathbf{z}_l^T \Sigma_l^{-1} \mathbf{z}_l}{2} \right),$$

where $C = -\frac{(nk+nd)}{2} \log(2\pi)$ is a constant.

In the E step, we calculate the expectation of the joint log-likelihood function with respect to the distribution of \mathbf{Z} conditional on observations \mathbf{Y} , and the current estimate of parameters, denoted as $\hat{\Theta} = (\hat{\mathbf{U}}_0, \hat{\sigma}_0^2, \hat{\boldsymbol{\rho}}, \hat{\boldsymbol{\sigma}}^2)$. The posterior distribution of factors given $\hat{\Theta}$ follows a multivariate Gaussian distribution (Gu and Shen, 2020):

$$(10) \quad (\mathbf{z}_l | \mathbf{Y}, \hat{\Theta}) \sim \mathcal{MN} \left(\hat{\mathbf{z}}_l, \hat{\sigma}_0^2 \hat{\Sigma}_l (\hat{\Sigma}_l + \hat{\sigma}_0^2 \mathbf{I}_n)^{-1} \right),$$

where $\hat{\mathbf{z}}_l = \hat{\Sigma}_l (\hat{\Sigma}_l + \hat{\sigma}_0^2 \mathbf{I}_n)^{-1} \tilde{\mathbf{y}}_l$ for $l = 1, \dots, d$, with $\tilde{\mathbf{Y}} = \mathbf{U}_0^T \mathbf{Y} = [\tilde{\mathbf{y}}_1, \dots, \tilde{\mathbf{y}}_d]^T$ being the projected observation matrix. Denote $\hat{\mathbf{Z}} = [\hat{\mathbf{z}}_1, \dots, \hat{\mathbf{z}}_d]^T$, a $d \times n$ matrix of the posterior mean of latent factors and $\bar{\ell}(\Theta) = \mathbb{E}_{\mathbf{Z} | \mathbf{Y}, \hat{\Theta}}[\ell(\Theta)]$. Utilizing Equation (10), the E step follows

$$(11) \quad \begin{aligned} \bar{\ell}(\Theta) = C + \frac{\operatorname{tr}(\mathbf{Y}^T \mathbf{U}_0 \hat{\mathbf{Z}})}{\sigma_0^2} - \sum_{l=1}^d \left\{ \frac{\log |\Sigma_l|}{2} + \frac{\hat{\mathbf{z}}_l^T \hat{\mathbf{z}}_l + \operatorname{tr}[\hat{\sigma}_0^2 \hat{\Sigma}_l (\hat{\Sigma}_l + \hat{\sigma}_0^2 \mathbf{I}_n)^{-1}]}{2\sigma_0^2} \right\} \\ - \sum_{l=1}^d \frac{\hat{\mathbf{z}}_l^T \Sigma_l^{-1} \hat{\mathbf{z}}_l + \operatorname{tr}[\hat{\sigma}_0^2 \Sigma_l^{-1} \hat{\Sigma}_l (\hat{\Sigma}_l + \hat{\sigma}_0^2 \mathbf{I}_n)^{-1}]}{2} - \frac{nk}{2} \log(\sigma_0^2) - \frac{\operatorname{tr}(\mathbf{Y}^T \mathbf{Y})}{2\sigma_0^2}, \end{aligned}$$

where Σ_l depends on unknown (ρ, σ^2) to be optimized, whereas $\hat{\Sigma}_l$ is obtained based on the current estimate of the parameters $(\hat{\rho}, \hat{\sigma}^2)$.

Directly computing the conditional distribution in Equation (10) requires $\mathcal{O}(dn^3)$ operations due to inverting d matrices of size $n \times n$, which can be computationally expensive. Instead, by treating the projected observations $\tilde{\mathbf{y}}_l = (\tilde{y}_l(1), \dots, \tilde{y}_l(n))^T$ as the noisy observations of the l th latent process, we can apply KF and RTS smoother independently to each latent factor. This approach efficiently computes the required quantities with $\mathcal{O}(dn)$ operations, avoiding the need for matrix inversion. Lemma 2.4 demonstrates their roles in simplifying computations in the E step.

LEMMA 2.4. *Consider a dynamic linear model with output $\tilde{y}_l(t) = z_l(t) + \epsilon$ and latent factor process defined in (4), with ϵ being an independent noise with variance σ_0^2 for $l = 1, \dots, d$. Denote $s_l(t) = \mathbb{E}[z_l(t) | \tilde{\mathbf{y}}_l, \hat{\Theta}]$, $S_l(t) = \mathbb{V}[z_l(t) | \tilde{\mathbf{y}}_l, \hat{\Theta}]$ and $\tilde{S}_l(t) = \text{Cov}[z_l(t), z_l(t+1) | \tilde{\mathbf{y}}_l, \hat{\Theta}]$, which can be computed by the KF and RTS smoother in $\mathcal{O}(n)$ operations. By leveraging the tridiagonal structure of Σ_l^{-1} , we have*

$$(12) \quad \text{tr}[\hat{\sigma}_0^2 \hat{\Sigma}_l (\hat{\Sigma}_l + \hat{\sigma}_0^2 \mathbf{I}_n)^{-1}] = \sum_{t=1}^n \mathbb{V}[z_l(t) | \mathbf{Y}, \hat{\Theta}] = \sum_{t=1}^n S_l(t),$$

$$(13) \quad \hat{\mathbf{z}}_l^T \Sigma_l^{-1} \hat{\mathbf{z}}_l = \frac{1}{\sigma_l^2} \left((1 - \rho_l^2) s_l(1) + \sum_{t=2}^n (s_l(t) - \rho_l s_l(t-1))^2 \right),$$

$$(14) \quad \text{tr}[\hat{\sigma}_0^2 \Sigma_l^{-1} \hat{\Sigma}_l (\hat{\Sigma}_l + \hat{\sigma}_0^2 \mathbf{I}_n)^{-1}] = \frac{1}{\sigma_l^2} \left(\sum_{t=1}^n S_l(t) + \rho_l^2 \sum_{t=2}^{n-1} S_l(t) - 2\rho_l \sum_{t=1}^{n-1} \tilde{S}_l(t) \right).$$

In the M step, the parameters $\hat{\Theta}^{\text{new}} = (\hat{\mathbf{U}}_0^{\text{new}}, (\hat{\sigma}_0^2)^{\text{new}}, \hat{\rho}^{\text{new}}, (\hat{\sigma}^2)^{\text{new}})$ are obtained by

$$(15) \quad \hat{\Theta}^{\text{new}} = \arg\max_{\Theta} \bar{\ell}(\Theta).$$

We emphasize that all parameters have closed-form expressions in the M-step in (15), thus avoiding numerically optimizing the high-dimensional parameter space in the algorithm. An efficient update in M-step is given in Theorem 2.5.

THEOREM 2.5. *Given the parameters estimated from the last iteration, one can compute $\{s_l(t)\}_{t=1}^n$, $\{S_l(t)\}_{t=1}^n$ and $\{\tilde{S}_l(t)\}_{t=1}^{n-1}$ by the KF and RTS smoother, for $l = 1, \dots, d$. The closed-form expression of $\hat{\Theta}^{\text{new}}$ from the M step, as defined in (15), are given below.*

1. Update $\hat{\mathbf{U}}_0^{\text{new}}$ by

$$(16) \quad \hat{\mathbf{U}}_0^{\text{new}} = \tilde{\mathbf{V}} \tilde{\mathbf{U}}^T,$$

where $\tilde{\mathbf{U}}$ and $\tilde{\mathbf{V}}$ being the left and right singular vectors of the $\hat{\mathbf{Z}} \mathbf{Y}^T$, respectively.

2. Update $(\hat{\sigma}_0^2)^{\text{new}}$ by

$$(17) \quad (\hat{\sigma}_0^2)^{\text{new}} = \frac{\text{tr}(\mathbf{Y}^T \mathbf{Y}) - 2 \text{tr}(\mathbf{Y}^T \hat{\mathbf{U}}_0^{\text{new}} \hat{\mathbf{Z}}) + \sum_{l=1}^d \sum_{t=1}^n (s_l^2(t) + S_l(t))}{nk}.$$

3. Update $\hat{\rho}_l^{\text{new}}$ by solving the following cubic equation in the interval $(-1, 1)$ which has a unique root in $(-1, 1)$ if $\hat{\sigma}_0^2 > 0$ and $\hat{\sigma}_l^2 > 0$:

$$(18) \quad \beta_0 + \beta_1 \rho_l + \beta_2 \rho_l^2 + \beta_3 \rho_l^3 = 0,$$

where $\beta_0 = n \left(\sum_{t=2}^n s_l(t-1) s_l(t) + \sum_{t=1}^{n-1} \tilde{S}_l(t) \right)$, $\beta_1 = - \sum_{t=1}^n s_l^2(t) - \sum_{t=1}^n S_l(t) - n \sum_{t=2}^{n-1} s_l^2(t) - n \sum_{t=2}^{n-1} S_l(t)$, $\beta_2 = (2 - n) \left(\sum_{t=2}^n s_l(t-1) s_l(t) + \sum_{t=1}^{n-1} \tilde{S}_l(t) \right)$, $\beta_3 = (n - 1) \left(\sum_{t=2}^{n-1} s_l^2(t) + \sum_{t=2}^{n-1} S_l(t) \right)$.

Algorithm 1 Fast EM algorithm for multivariate Ornstein-Uhlenbeck process

Input: $k \times n$ observation matrix \mathbf{Y} , time step $1, 2, \dots, n$ and selected number of latent processes d . The representer \mathbf{G} and noise level σ_0^2 should be provided if they are fixed.

- 1: (Optional) Initialize \mathbf{U}_0 and σ_0^2 if they are unspecified.
 - 2: Initialize $(\hat{\boldsymbol{\rho}}, \hat{\boldsymbol{\sigma}}^2)$ and then apply KF and RTS smoother to get $\{s_l(t)\}_{t=1}^n, \{S_l(t)\}_{t=1}^n$ and $\{\tilde{S}_l(t)\}_{t=1}^{n-1}$ for $l = 1, \dots, d$.
 - 3: **while** The convergence criteria were not met and the number of iterations is less than the upper bound **do**
 - 4: (Optional.) If \mathbf{U}_0 is unknown, update $\hat{\mathbf{U}}_0$ using Equation (16).
 - 5: (Optional.) If σ_0^2 is unknown, update $\hat{\sigma}_0^2$ using Equation (17).
 - 6: Update $\hat{\rho}_l$ in the correlation matrix \mathbf{R}_l for $l = 1, \dots, d$ using Equation (18).
 - 7: Update $\hat{\sigma}_l^2$ for $l = 1, \dots, d$ using Equation (19).
 - 8: Update $\{s_l(t)\}_{t=1}^n, \{S_l(t)\}_{t=1}^n, \{\tilde{S}_l(t)\}_{t=1}^{n-1}$ and $\hat{\mathbf{Z}}$ by KF and RTS smoother.
 - 9: **end while**
- Output:** Θ^{MMLE} and \mathbf{Z}^{post} .

4. Update $(\hat{\sigma}_l^2)^{\text{new}}$ by

$$(19) \quad (\hat{\sigma}_l^2)^{\text{new}} = \frac{1}{n} \left\{ (1 - (\hat{\rho}_l^{\text{new}})^2) s_l(1) + \sum_{t=2}^n (s_l(t) - \hat{\rho}_l^{\text{new}} s_l(t-1))^2 \right\} + \frac{1}{n} \left\{ \sum_{t=1}^n S_l(t) + (\hat{\rho}_l^{\text{new}})^2 \sum_{t=2}^{n-1} S_l(t) - 2\hat{\rho}_l^{\text{new}} \sum_{t=1}^{n-1} \tilde{S}_l(t) \right\}.$$

5. Update $\{s_l^{\text{new}}(t)\}_{t=1}^n, \{S_l^{\text{new}}(t)\}_{t=1}^n$ and $\{\tilde{S}_l^{\text{new}}(t)\}_{t=1}^{n-1}$ by KF and RTS smoother using $\hat{\Theta}^{\text{new}}$. Set $\hat{\mathbf{z}}_l^{\text{new}} = [s_l^{\text{new}}(1), \dots, s_l^{\text{new}}(n)]^T$ and $\hat{\mathbf{Z}}^{\text{new}} = [\hat{\mathbf{z}}_1^{\text{new}}, \dots, \hat{\mathbf{z}}_d^{\text{new}}]^T$.

For our application of slip estimation from GPS data, the latent loading matrix is computed by Green's function, and the variance of the noise is usually available from GPS measurement in practice. The FMOU is applicable to this scenario as well, discussed in Section S3.5 in the supplementary materials. Algorithm 1 summarizes our FMOU approach.

The output of Algorithm 1 is the MMLE of the parameters Θ^{MMLE} in (8) and posterior mean of the latent factors given Θ^{MMLE} , denoted as $\mathbf{Z}^{\text{post}} = [\mathbf{z}^{\text{post}}(1), \dots, \mathbf{z}^{\text{post}}(n)] = \mathbb{E}[\mathbf{Z} | \mathbf{Y}, \Theta^{\text{MMLE}}]$. In our application of slip estimation, other quantities, such as the posterior distribution of the mean of the observations and slips at time t follows

$$(20) \quad (\mathbf{m}(t) | \mathbf{Y}, \Theta^{\text{MMLE}}) \sim \mathcal{MN}(\mathbf{U}_0 \mathbf{z}^{\text{post}}(t), \boldsymbol{\Sigma}_m^{\text{MMLE}}(t)),$$

$$(21) \quad (\mathbf{z}_s(t) | \mathbf{Y}, \Theta^{\text{MMLE}}) \sim \mathcal{MN}(\mathbf{G}^T \mathbf{U}_0 \mathbf{D}_0^{-2} \mathbf{z}^{\text{post}}(t), \boldsymbol{\Sigma}_s^{\text{MMLE}}(t)),$$

where $\boldsymbol{\Sigma}_m^{\text{MMLE}}(t) = \mathbf{U}_0 \mathbf{D}_S(t) \mathbf{U}_0^T$ and $\boldsymbol{\Sigma}_s^{\text{MMLE}}(t) = \mathbf{G}^T \mathbf{U}_0 \mathbf{D}_0^{-2} \mathbf{D}_S(t) \mathbf{D}_0^{-2} \mathbf{U}_0^T \mathbf{G}$, with $\mathbf{D}_S(t)$ being a $d \times d$ diagonal matrix where the l th element is $S_l(t)$ computed by plugging in the MMLE of the parameters for $l = 1, 2, \dots, d$. Here \mathbf{U}_0 can be either fixed or estimated. In the application of slip estimation, \mathbf{U}_0 and \mathbf{D}_0 are the first d left singular vectors and the largest d singular values of the matrix of Green's function \mathbf{G} , respectively.

Several advantages of this EM algorithm are worth mentioning. First, the kernel parameters in Gaussian processes are notoriously hard to estimate numerically, and we have d sets of kernel and scale parameters, where d can be on the order of 10^3 or even 10^6 in practice. The estimates of these parameters have closed-form expressions in our EM algorithm, which had not been derived before. Our algorithm substantially improves estimation stability compared to optimization algorithms that numerically optimize in a high-dimensional parameter space. Second, when \mathbf{U}_0 is unknown and the parameters are distinct in each latent process, originally one needs to solve a constrained optimization problem in the Stiefel manifold (Wen

and Yin, 2013) to optimize \mathbf{U}_0 in each of the numerical iteration for estimating the parameters of the model in (3) and (4) (Gu and Shen, 2020). In contrast, we derived closed-form expressions for estimating \mathbf{U}_0 in each iteration of the EM algorithm, and hence the algorithm is much faster. Third, we integrate orthogonal projection in KF and RTS smoother to bypass the matrix inversion operation at each time step. For M iterations of the EM algorithms, the overall complexity of the parameter estimation process is $\mathcal{O}(Mknd) + \mathcal{O}(Mkd^2)$ when the coefficient \mathbf{U}_0 is unknown. For the scenario where \mathbf{U}_0 is derived from the Green's function, we need to perform SVD to obtain \mathbf{U}_0 , which has the order $\mathcal{O}(\min(k^2k', k(k')^2))$.

2.3. Estimation of the number of latent processes. Estimating a suitable number of factors is crucial to distinguish signals from noise. Various approaches have been developed based on, for instance, information criteria (Bai and Ng, 2002), the cumulative percentage of variance explained by the factors (Hotelling, 1933), and the ratio of neighboring eigenvalues of the empirical autocovariance matrix (Lam et al., 2011). In our scientific application, the goal is not to select the number of factors, but to provide a suitable model for linking the complex slip propagation process to ground deformation. To enable the variability in the signal to be properly explained by our model, we select the number of latent factors, d , by minimizing the difference between the estimated and measured noise variance:

$$(22) \quad \hat{d} = \operatorname{argmin}_d |(\sigma_0^{\text{MMLE}}(d))^2 - \sigma_0^2|,$$

where σ_0^2 is the measured variance of the noise from GPS, and $(\sigma_0^{\text{MMLE}}(d))^2$ is the estimated variance of the noise with d latent factors. We call this approach variance matching (VM).

When the variance of the noise is unknown, we use an information criterion to select the number of factors (Bai and Ng, 2002), which often has the form below:

$$(23) \quad \hat{d} = \operatorname{argmin}_d \left\{ \log(\|\mathbf{Y} - \tilde{\mathbf{U}}_{1:d} \tilde{\mathbf{U}}_{1:d}^T \mathbf{Y}\|_F) + C(k, n) \right\},$$

where $\|\cdot\|_F$ denotes the Frobenius matrix norm, $\tilde{\mathbf{U}}_{1:d}$ is the first d columns from the left unitary matrix of the singular value decomposition of \mathbf{Y} and $C(k, n)$ is a penalty term, such as $C(k, n) = d \left(\frac{k+n}{kn} \right) \log\left(\frac{kn}{k+n} \right)$. This approach will be compared in Section 4.

3. Improved computational scalability and efficiency. We discuss the connection to several other approaches, including the dynamic mode decomposition (DMD) (Schmid, 2010) in Section 3.1, and the generalized probabilistic principal component analysis (GP-PCA) (Gu and Shen, 2020) in Section 3.2. For estimating slips from geodetic data, the network inversion filter (NIF) (Segall and Matthews, 1997) and its modification (Bartlow et al., 2011) are a class of vector autoregressive models, summarized in Section S4 in the supplementary materials. The computational order of different approaches is provided in Table 1.

3.1. The FMOU approach extends the dynamic mode decomposition with a symmetric transition matrix for noisy data. The DMD is a popular approach in computational mathematics to obtain the reduced-rank representation of nonlinear dynamical systems (Schmid, 2010; Tu et al., 2014). In DMD, one approximates a real-valued output of k dimensions at time t through $\mathbf{y}(t) \approx \mathbf{A}\mathbf{y}(t-1)$, where \mathbf{A} is a $k \times k$ linear transition matrix, estimated by

$$(24) \quad \hat{\mathbf{A}} = \operatorname{argmin}_{\mathbf{A}} \|\mathbf{Y}_{2:n} - \mathbf{A}\mathbf{Y}_{1:n-1}\| = \mathbf{Y}_{2:n} \mathbf{Y}_{1:n-1}^+,$$

where $\mathbf{Y}_{2:n} = [\mathbf{y}(2), \dots, \mathbf{y}(n)]$, $\mathbf{Y}_{1:n-1} = [\mathbf{y}(1), \dots, \mathbf{y}(n-1)]$, $\|\cdot\|$ stands for the L_2 or Frobenius norm, and $\mathbf{Y}_{2:n}^+$ represents the Moore-Penrose pseudo-inverse of $\mathbf{Y}_{2:n}$.

Estimating the leading eigenpairs of \mathbf{A} is crucial for finding the low-rank representation of the system. In Tu et al. (2014), the authors proposed an efficient algorithm named exact

Methods	computational order	a noise model	closed-form expressions of \mathbf{U}_0
FMOU	$\mathcal{O}(Mknd) + \mathcal{O}(Mkd^2)$	Yes	Yes
DMD	$\min(\mathcal{O}(kn^2), \mathcal{O}(k^2n))$	No	Yes
GPPCA	$\mathcal{O}(M_1M_2knd) + \mathcal{O}(M_1M_2kd^2)$	Yes	No
NIF	$\mathcal{O}(\tilde{M}k^3n)$	Yes	/

TABLE 1

Comparison of different approaches by the computational order, whether a noise model is included, and whether a close-formed expression in estimating the factor loading matrix is available when the factor processes have distinct correlation parameters. For FMOU, we assume M iterations in EM, where $M \approx 10$ s often achieve good performance. For DMD, we only consider the cost of obtaining the first d eigenvectors, whereas obtaining the transition coefficient matrix requires extra $\mathcal{O}(k^2d)$ operations. When each factor contains distinct correlation parameters, GPPCA requires M_1 iterations and each requires M_2 steps to optimize the factor loading matrix in the Stiefel manifold. To estimate the slip, an additional SVD operation of a $k \times k'$ matrix \mathbf{G} is needed and it only needs to be done once. Thus, the order of FMOU is $\mathcal{O}(\min(k^2k', k(k')^2)) + \mathcal{O}(Mknd)$ and the order of NIF is $\mathcal{O}(\min(k^2k', k(k')^2)) + \mathcal{O}(\tilde{M}k^3n)$ with \tilde{M} being the number of iterations in NIF for slip estimation.

DMD, which identifies the nonzero eigenvalues and the corresponding eigenvectors of \mathbf{A} with $\min(\mathcal{O}(kn^2), \mathcal{O}(nk^2))$ operations. The exact DMD algorithm is summarized in Section S4.1 in the supplementary materials.

A probabilistic model of the DMD was introduced in Gu et al. (2024b), which shows the estimation of \mathbf{A} in DMD is equivalent to the maximum likelihood estimator of \mathbf{A} in the vector autoregressive model $\mathbf{y}(t) = \mathbf{A}\mathbf{y}(t-1) + \tilde{\mathbf{w}}(t)$, where $\tilde{\mathbf{w}}(t) \sim \mathcal{MN}(\mathbf{0}, \Sigma_{\tilde{\mathbf{w}}})$ represents the innovation with a positive definition matrix $\Sigma_{\tilde{\mathbf{w}}}$. However, both DMD and its probabilistic model assume noise-free observation, which is restrictive in practice.

The FMOU model includes an additional level of noise modeling for DMD with a symmetric transition matrix. To see this, for the FMOU model in (3) and (4), denoting $\bar{\mathbf{z}}(t) = \mathbf{U}_0\mathbf{z}(t)$, the model can be equivalently written as

$$(25) \quad \mathbf{y}(t) = \bar{\mathbf{z}}(t) + \boldsymbol{\epsilon}(t),$$

$$(26) \quad \bar{\mathbf{z}}(t) = \mathbf{A}\bar{\mathbf{z}}(t-1) + \tilde{\mathbf{w}}(t),$$

where $\mathbf{A} = \mathbf{U}_0\Lambda_\rho\mathbf{U}_0^T$ with \mathbf{U}_0 being an $k \times d$ orthogonal matrix and Λ_ρ being an $d \times d$ diagonal matrix having the l th diagonal entry ρ_l , and $\tilde{\mathbf{w}}(t) \sim \mathcal{N}(\mathbf{0}, \Sigma_{\tilde{\mathbf{w}}})$ with $\Sigma_{\tilde{\mathbf{w}}} = \mathbf{U}_0\mathbf{D}_\sigma\mathbf{U}_0^T$ being a $k \times k$ matrix, and $\mathbf{D}_\sigma = \text{diag}(\sigma_1^2, \dots, \sigma_d^2)$. By multiplying \mathbf{U}_0^T on both sides of Equations (25)-(26), we obtain the FMOU model.

Thus the FMOU approach provides a fast solution of a noise-inclusive, probabilistic DMD model with a symmetric transition matrix. This extension drastically improves the DMD when the data contain noises, as will be numerically demonstrated in Section 4. The computational order of DMD and FMOU is summarized in Table 1, and both are fast in practice. When both k and n are large, the FMOU can be faster than the DMD.

3.2. The FMOU approach enables scalable and robust estimation for the generalized probabilistic principal component analysis. The FMOU model is connected to the GPPCA approach (Gu and Shen, 2020), which assumes each latent factor follows a Gaussian process. However, when the variance and range parameters of the latent processes are distinct, in each iteration of the parameter estimation, one needs to apply an iterative algorithm to estimate the factor loading matrix on the Stiefel manifold (Wen and Yin, 2013). In total, one needs M_1M_2 iterations, where M_1 are for numerical optimization of the parameters, each requiring M_2 iterations to optimize the factor loading matrix. This process can be prohibitively expensive. Furthermore, numerical optimization of d sets of range and variance parameters can also be unstable. In FMOU, we only need M EM iterations, as the estimation of parameters

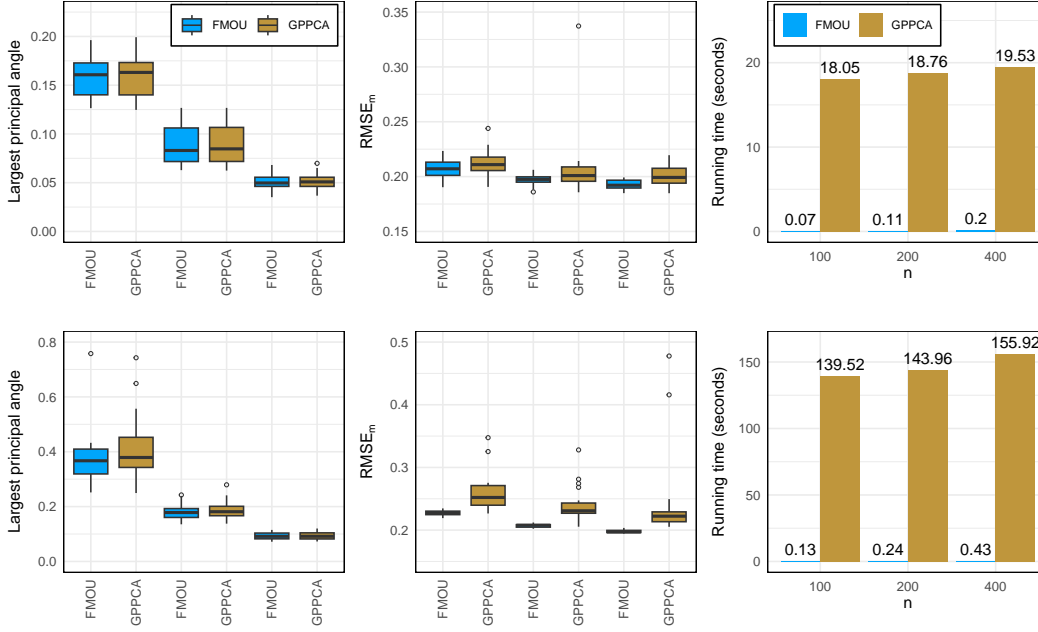


Figure 1: The largest principal angle between the true loading matrix \mathbf{U}_0 and its estimates, the $RMSE_m$ and the running time of performing models in Experiment 1 with correctly specified number of latent factors in FMOU and GPPCA. The first and second rows show the scenarios with $(k=20, d=5)$ and $(k=40, d=10)$, respectively. The first 2, middle 2, and last 2 boxes are associated with $n=100$, $n=200$, and $n=400$, respectively, in each figure.

have closed-form expressions. We use Experiment 1 to numerically compare the stability and computational speed of FMOU and GPPCA.

EXPERIMENT 1. *The data are generated by Equations (3)-(4). The orthogonal matrix $\mathbf{U}_0 \in \mathbb{R}^{k \times d}$ is sampled from the Stiefel manifold with two configurations with $(k=20, d=5)$ and $(k=40, d=10)$, where d is assumed to be known. The latent factors are generated with inputs $t=1, \dots, n$ for three scenarios with $n \in \{100, 200, 400\}$. The parameters ρ_l and σ_l^2 are sampled from $Unif(0.95, 1)$ and $Unif(0.5, 1)$ for $l=1, \dots, d$, respectively, and the variance of the noise is $\sigma_0^2 = 0.2$. We repeat the simulation $N=20$ times under each configuration.*

We use two criteria to evaluate the estimation of the latent factor loadings and the mean. First, we compute the largest principal angle ϕ_d between $\mathcal{M}(\hat{\mathbf{U}}_0)$ and $\mathcal{M}(\mathbf{U}_0)$, the linear subspaces spanned by the estimation $\hat{\mathbf{U}}_0$ and by the truth \mathbf{U}_0 , respectively, to measure the closeness of two linear subspaces. Let $0 \leq \phi_1 \leq \dots \leq \phi_d \leq \pi/2$ be the principal angles:

$$(27) \quad \phi_l = \arccos \left(\max_{\mathbf{u} \in \mathcal{M}(\mathbf{U}_0), \hat{\mathbf{u}} \in \mathcal{M}(\hat{\mathbf{U}}_0)} |\mathbf{u}^T \hat{\mathbf{u}}| \right) = \arccos(|\mathbf{u}_l^T \hat{\mathbf{u}}_l|),$$

such that $\|\mathbf{u}\| = \|\hat{\mathbf{u}}\| = 1$, $\mathbf{u}^T \mathbf{u}_l = \hat{\mathbf{u}}^T \hat{\mathbf{u}}_l = 0$, with \mathbf{u}_l and $\hat{\mathbf{u}}_l$ being the l th column of \mathbf{U}_0 and $\hat{\mathbf{U}}_0$ for $l=1, \dots, d-1$.

Second, we compute the root of the mean squared error for the mean of the observations:

$$RMSE_m = \frac{1}{N} \sqrt{\frac{\sum_{i=1}^k \sum_{t=1}^n (\hat{y}_i(t) - \mathbb{E}[y_i(t)])^2}{kn}},$$

where $\hat{y}_i(t)$ is the predictive mean of $y_i(t)$ and N is the number of replications.

Figure 1 compares FMOU with GPPCA. The largest principal angles between the exact loading matrix and its estimations from FMOU and GPPCA are close. The FMOU is consistently better than the GPPCA in estimating the mean, and the effect is more pronounced for $d = 10$, a larger dimension of the latent space. This is because numerically optimizing a large number of parameters and factor loading matrix leads to a larger error from GPPCA, whereas such a problem is overcome by closed-form expressions in each EM iteration in FMOU. Furthermore, the FMOU is much faster than the GPPCA shown in the right panels in Figure 1, as the estimation of factor loadings has a closed-form solution in FMOU, yet numerical optimization in Stiefel manifold is required in each optimization step in GPPCA.

Hence, FMOU achieves tremendous improvements in terms of scalability and efficiency for the model in (3)-(4), compared to GPPCA. In Section 4, we use extensive examples with correctly specified or misspecified scenarios to compare FMOU with other approaches.

4. Simulated experiments. In this section, we numerically compare our method with alternative approaches by simulation. The experiments are split into two subsections. The scenarios with an estimated factor loading matrix are considered in Section 4.1, whereas Section 4.2 focuses on cases with a fixed factor loading matrix. Both correctly specified models and misspecified models are considered. In Section 4.1, we compared with DMD and two data-driven latent factor models, denoted as LY1 and LY5, introduced in Lam and Yao (2012). In the LY1 and LY5 methods, the number of latent factors \hat{d} is first estimated by minimizing the ratio of neighboring eigenvalues of $\mathbf{C} := \sum_{p=1}^{p_0} \hat{\Sigma}_y(p) \hat{\Sigma}_y^T(p)$, with $p_0 = 1$ for LY1 and $p_0 = 5$ for LY5, where $\hat{\Sigma}_y(p)$ denotes the sample covariance matrix with a lag time p . In both methods, the factor loading matrix \mathbf{U}_0 is estimated by the first d eigenvectors of \mathbf{C} corresponding to the largest d eigenvalues. Results with an estimated latent factor loading matrix \hat{d} are shown in Section S5 in supplementary materials. In Section 4.2, we construct two additional experiments where the factor loadings are either sampled from the Stiefel manifold or derived from the singular vectors of the Green's function used in real data, mimicking the slip propagation process. We compare FMOU with NIF (Segall and Matthews, 1997) for these two experiments. Other than estimation error and computational time, we also record the proportion of the signals and slips covered in 95% posterior credible intervals and the average length of the intervals of the FMOU approach in Tables S2-S6 in supplementary materials, yet these uncertainty measures are not available for other methods, such as DMD.

4.1. *Simulated experiments with estimated factor loadings.* We first study Experiment 2, where all parameters, $(\mathbf{U}_0, \sigma_0^2, \sigma^2, \rho)$, are estimated.

EXPERIMENT 2 (Correctly specified models with estimated factor loading matrices). *The data are generated by Equations (3)-(4) with the orthogonal matrix $\mathbf{U}_0 \in \mathbb{R}^{k \times d}$ sampled from the Stiefel manifold with $k = 20$ and $d = 5$. Here ρ_l and σ_l^2 are sampled from $\text{Unif}(0.95, 1)$ and $\text{Unif}(0.5, 1)$ for $l = 1, \dots, d$, respectively. Six scenarios with three different numbers of the time points $n \in \{100, 200, 400\}$ and two unobserved variances of the noise $\sigma_0^2 \in \{1, 2\}$ are considered. We repeat the simulation $N = 20$ times for each scenario.*

In Figure 2, we show the largest principal angle of factor loading matrix \mathbf{U}_0 for all approaches with a correctly specified d . Across all scenarios, the estimation by the FMOU approach has the smallest principal angles between the estimated and true loading factor loading matrix. In Figure S1 in the supplementary materials, we show that the number of latent factors can be correctly estimated by the information criterion (IC) in Equation (23), and the estimation is more accurate than the alternatives.

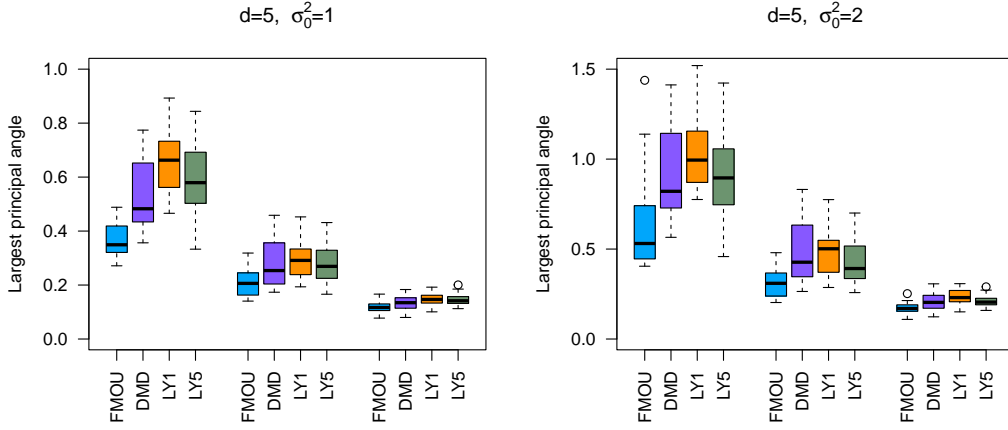


Figure 2: The largest principal angle (from 0 to $\pi/2$) between the true loading matrix \mathbf{U}_0 and its estimates from 4 methods in Experiment 2 with correctly specified latent factors. The variance of the noise is assumed to be $\sigma_0^2 = 1$ and $\sigma_0^2 = 2$ for the left and right panels, respectively. In each panel, the first 4, middle 4, and last 4 boxes are associated with a different number of time points, $n = 100$, $n = 200$, and $n = 400$, respectively.

$d = 5$	$\sigma_0^2 = 1$			$\sigma_0^2 = 2$		
	$n = 100$	$n = 200$	$n = 400$	$n = 100$	$n = 200$	$n = 400$
FMOU	0.379	0.348	0.334	0.498	0.436	0.414
DMD	0.629	0.629	0.634	0.765	0.761	0.766
LY1	0.913	0.577	0.569	1.303	0.831	0.814
LY5	0.889	0.572	0.575	1.257	0.814	0.814

TABLE 2

Average of $RMSE_m$ over N repeats of Experiment 2 with the truth $d = 5$.

The $RMSE_m$ in estimating the mean of the data of Experiment 2 is shown in Table 2. The FMOU achieves higher accuracy under all combinations with different n and σ_0^2 . In Figure 3, we plot the observations, the mean, and estimation by different methods for $\sigma_0^2 = 1$ and $\sigma_0^2 = 2$. The predictive mean from FMOU is close to the truth, plotted as black curves, and the 95% posterior credible interval of the mean covers the truth most of the time.

EXPERIMENT 3 (Misspecified models with estimated factor loading matrices). (1) *Linear diffusion (Carslaw, 1906)*. The signal is governed by the partial differential equation $\frac{\partial u(x,t)}{\partial t} = D \frac{\partial^2 u(x,t)}{\partial x^2}$, where $u(x,t)$ represents the concentration of the diffusing material at location x and time t , and D is the diffusion coefficient. We follow Lu and Tarakovsky (2020) to let $D = 1$, discretize the spatial domain $[0, 1]$ into 500 equally spaced grid points, $u(x, 0) = 0$, and let a boundary condition be applied at one end with a constant external concentration of 1. The signal is generated over a time interval $t \in [0, 0.2]$ using $n = 500$ with a numerical solver (Soetaert et al., 2010). Three noise variances $\sigma_0^2 \in \{0.01^2, 0.05^2, 0.3^2\}$ are tested. (2) *Lorenz 96 system (Lorenz, 1996)*. The signal follows $\frac{df_m(t)}{dt} = (f_{m+1}(t) - f_{m-2}(t))f_{m-1}(t) - f_m(t) + F$, for $m = 1, \dots, 40$ and $F = 8$. We generate the signal using the fourth-order Runge Kutta method with a step size 0.01 for $n = 500$ time steps and three noise variances $\sigma_0^2 \in \{0.1, 0.5, 1\}$ are included to generate observations. We repeat the simulation $N = 20$ times for each scenario.

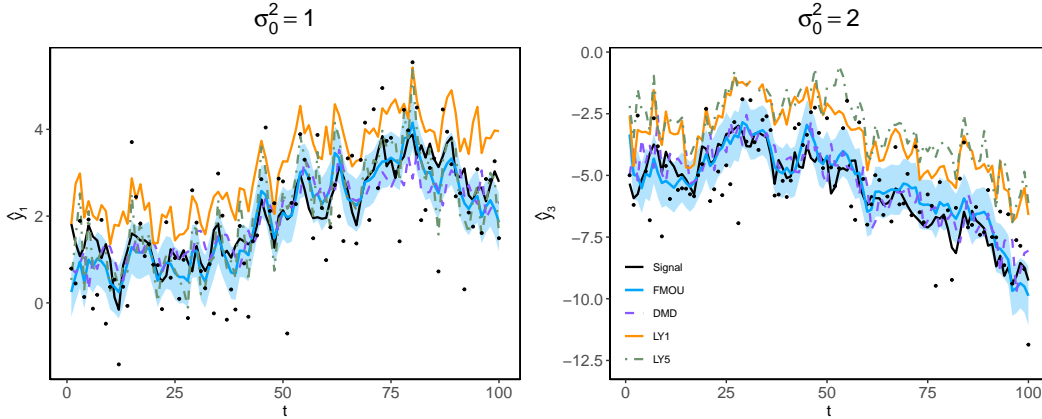


Figure 3: Predictive mean by FMOU (solid blue curves), DMD (dashed purple curve), LY1 (solid orange curves) and LY5 (dashed green curves), from one repetition in Experiment 2. The observations and mean of the observations are plotted by the black circles and curves, respectively. The blue-shaded area is the 95% posterior credible interval given by FMOU.

	Linear diffusion			Lorenz 96		
	$\sigma_0^2 = 0.01^2$	$\sigma_0^2 = 0.05^2$	$\sigma_0^2 = 0.3^2$	$\sigma_0^2 = 0.1$	$\sigma_0^2 = 0.5$	$\sigma_0^2 = 1$
FMOU	1.67×10^{-3}	6.96×10^{-3}	3.39×10^{-2}	0.185	0.325	0.418
DMD	9.41×10^{-3}	4.68×10^{-2}	2.85×10^{-1}	0.280	0.571	0.770
LY1	1.10×10^{-1}	7.12×10^{-2}	3.00×10^{-1}	0.666	0.942	1.114
LY5	1.00×10^{-2}	5.01×10^{-2}	3.00×10^{-1}	1.696	2.254	2.417

TABLE 3

Average of $RMSE_m$ over $N = 20$ repeats of Experiment 3.

Table 3 presents the average $RMSE_m$ for signal estimation over $N = 20$ simulations across various approaches. The results show that FMOU consistently achieves better accuracy under all noise levels, particularly excelling in large-noise scenarios. Figures 4 and 5 provide the comparison between FMOU and the alternative approaches in estimating the signal from noisy observations generated by the linear diffusion equation and Lorenz 96 system, respectively. The signal estimated by FMOU closely aligns with the ground truth, while DMD exhibits larger deviations. Additionally, the 95% posterior credible intervals in Figure 5 correctly cover the true signal for most of the time steps.

4.2. *Simulated experiments with known factor loadings.* In this section, we assume that \mathbf{U}_0 is given by the SVD of Green’s function. The observations are related to the unobserved slip by Equation (2). We quantify the estimated error of slips by $RMSE_s$:

$$(28) \quad RMSE_s = \frac{1}{N} \sqrt{\frac{\sum_{t=1}^n (\hat{\mathbf{z}}_s(t) - \mathbf{z}_s(t))^T (\hat{\mathbf{z}}_s(t) - \mathbf{z}_s(t))}{k'n}},$$

where $\hat{\mathbf{z}}_s(t) = (\hat{z}_{s,1}(t), \dots, \hat{z}_{s,k'}(t))^T$ is the estimated slips at time t , computed by $\hat{\mathbf{z}}_s(t) = \mathbf{G}^T \mathbf{U}_0 \mathbf{D}_0^{-2} \hat{\mathbf{z}}(t)$ with $\hat{\mathbf{z}}(t)$ being the estimation of latent factors.

EXPERIMENT 4 (Correctly specified models with a known factor loading matrix). *The data are generated by Equations (3)-(4), and the slips are computed by Equation (2), which approximate the data generating system in Equation (1). The orthogonal matrices*

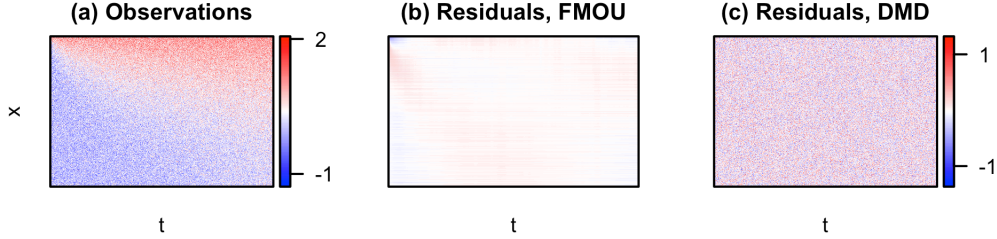


Figure 4: Noisy observations and predictive signals of the Linear diffusion example in Experiment 3. (a) Observations with large noise ($\sigma_0^2 = 0.3^2$). (b) Residuals between predictive signals by FMOU and the ground truth, i.e., $u(x, t) - \hat{u}_{\text{FMOU}}(x, t)$. (c) Residuals between predictive signals by DMD and the ground truth, i.e., $u(x, t) - \hat{u}_{\text{DMD}}(x, t)$. Subplots (b) and (c) share the same color key.

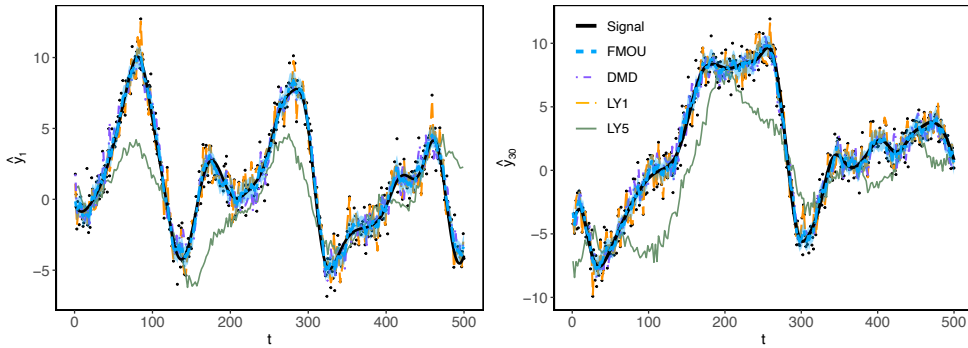


Figure 5: Predictive signals by FMOU (dashed blue curves), DMD (dot-dash purple curves), LY1 (long dash orange curves) and LY5 (solid green curves), from one simulation of Lorenz 96 system in Experiment 3 with $\sigma_0^2 = 1$. The black circles and solid black curves represent the observations and signals, respectively. The 95% posterior credible intervals by FMOU are graphed as the blue-shaded area. The left and right panels show the 1st and 30th states.

$\mathbf{U}_0 \in \mathbb{R}^{k \times k}$, $\mathbf{V}_0 \in \mathbb{R}^{k' \times k}$ are generated from the Stiefel manifold with two configurations: (1) $k = 25, k' = 150, d = 6$ and (2) $k = 32, k' = 100, d = 8$. The l th latent factor \mathbf{z}_l is generated with inputs $t = 1, \dots, n$ for $n \in \{100, 200, 300\}$. We have $\mathbf{D}_0 = \text{diag}(d_1, \dots, d_k)$ with d_l sampled from $\text{Unif}(0, 1)$ for $l = 1, \dots, k$ and rearranged decreasingly. Parameters ρ_l and σ_l^2 are sampled from $\text{Unif}(0.95, 1)$ and $\text{Unif}(1, 2)$, respectively, for $l = 1, \dots, d$. The matrix of the Green's function is constructed by $\mathbf{G} = \mathbf{U}_0 \mathbf{D}_0 \mathbf{V}_0^T$. The variance of the noise is assumed to be $\sigma_0^2 = 1.5$. We repeated simulation $N = 20$ times for each configuration.

We compare FMOU with NIF in this section, as other previously compared methods, such as DMD, LY1 and LY5, estimate the factor loading matrix. We show the RMSE_m and RMSE_s by FMOU and NIF in Figure 6. As NIF does not involve the selection of the number of factors d , to eliminate the effect of selecting d , we assume d is known for both FMOU and NIF. Across all configurations, the FMOU model consistently outperforms NIF in estimating the mean of the observations and the slip. Additionally, Figure S2 in supplementary materials compares the estimation of d in Experiment 4 and it demonstrates that IC can correctly identify the number of factors with a moderately large number of time points. The improvement by FMOU for Experiment 4 is not surprising as data are generated by FMOU model. Next we use a misspecified model in Experiment 5 to illustrate the flexibility of FMOU estimation.

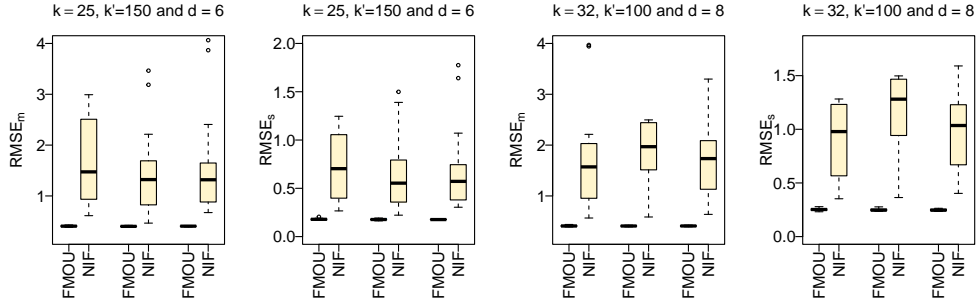


Figure 6: Box plots of RMSE_m and RMSE_s by FMOU and NIF in Experiment 4. The number of factors d is correctly specified for both FMOU and NIF. In each subfigure, the first 2, middle 2, and the last 2 boxes are based on $n = 100$, $n = 200$ and $n = 300$, respectively.

EXPERIMENT 5 (A misspecified latent factor model for estimating a 2D elliptical slip). *This simulation uses the Green’s tensor \mathbf{G} inherited from the real data for inferring the slip propagation in the Cascadia zone, where $k = 200$, $k' = 1978$, $n = 88$. An elliptical slip region is generated on a triangular mesh with a fixed center at $(\xi_{0,1}, \xi_{0,2}) = (123.2^\circ\text{W}, 46.0^\circ\text{N})$ and a fixed semi-minor axis extending from $(123.9^\circ\text{W}, 46.0^\circ\text{N})$ to $(122.5^\circ\text{W}, 46.0^\circ\text{N})$ with ground distance $r_0 = 108\text{km}$. The semi-major axis grows along the longitude as $r(t) = r_0/3 + vt$ with the growth rate $v = 8\text{km/day}$. Data is generated through model (1) and the slip at the h th fault patch $(\xi_{h,1}, \xi_{h,2})$ and time t is given by*

$$(29) \quad z_{s,h}(t) = z_{s,max}(1 - E(\boldsymbol{\xi}_h, t)^2) \times \mathbb{1}_{\{E(\boldsymbol{\xi}_h, t) \leq 1\}},$$

where $E(\boldsymbol{\xi}_h, t) = (\xi_{h,1} - \xi_{0,1})^2/r_0^2 + (\xi_{h,2} - \xi_{0,2})^2/r(t)^2$, $h = 1, \dots, k'$, $t = 1, \dots, n$. The slips have a peak value of $z_{s,max} = 3\text{cm}$ at the center and drop to zero outside the ellipse. We consider three configurations with known noise variances $\sigma_0^2 \in \{0.01^2, 0.02^2, 0.05^2\}\text{cm}^2$.

In Experiment 5, both \mathbf{U}_0 and σ_0^2 are known to mimic the application of the real data. We use the VM method in (22) to estimate the number of latent factors. Table 4 records the numerical comparisons between FMOU and NIF for Experiment 5. We consider two variants of NIF: one with $d = k$ and the other one with an estimated \hat{d} from IC. The FMOU achieves better accuracy in estimating both the mean of the observations and slips. Additionally, FMOU is considerably faster than the NIF model, as computing the likelihood function in FMOU only requires $\mathcal{O}(knd)$ operations. These orders do not consider SVD of Green’s function which only needs to be done once. Furthermore, as each step of EM algorithm has closed-form expressions, FMOU is also robust in estimating a large number of parameters.

Figure 7 graphs the 7-day averaged slips in centimeters, such that $\bar{z}_{s,h}(t) = \sum_{t'=0}^6 \hat{z}_{s,h}(t+t')/7$ for $h = 1, \dots, k'$. Both FMOU and NIF detect the front of ellipses and estimate slips’ propagation within the elliptical regions. The slips estimated by FMOU model align more closely with the truth which demonstrates the FMOU is more accurate in estimation.

5. Estimating slip propagation in Cascadia.

5.1. *Data and methods.* We employ GPS measurements to estimate slip rates within the Cascadia region, situated along the western edge of North America. The Cascadia region is characterized by the subduction of the Juan de Fuca plate beneath the North American plate. This geological interaction triggers slow slip events that last for weeks to months. The dataset used in this study is publicly available at the Plate Boundary Observatory, which

$\sigma_0^2 = 0.01^2$	\hat{d}	Avg. RMSE _m	Avg. RMSE _s	Running time (seconds)
FMOU	105	3.88×10^{-3}	2.25×10^{-1}	9.03
NIF	105	1.14×10^{-1}	6.41×10^{-1}	5.80×10^2
NIF	200	1.14×10^{-1}	6.41×10^{-1}	2.25×10^3
$\sigma_0^2 = 0.05^2$	\hat{d}	Avg. RMSE _m	Avg. RMSE _s	Running time (seconds)
FMOU	67	1.30×10^{-2}	3.37×10^{-1}	5.41
NIF	67	1.16×10^{-1}	6.57×10^{-1}	2.82×10^2
NIF	200	1.16×10^{-1}	6.57×10^{-1}	2.27×10^3
$\sigma_0^2 = 0.2^2$	\hat{d}	Avg. RMSE _m	Avg. RMSE _s	Running time (seconds)
FMOU	30	3.36×10^{-2}	4.82×10^{-1}	3.73
NIF	30	1.15×10^{-1}	6.67×10^{-1}	98.3
NIF	200	1.15×10^{-1}	6.60×10^{-1}	2.29×10^3

TABLE 4

Results for Experiment 5. The standard deviation of the mean of the output and the slip are 0.19 and 0.85, respectively. The major cost in FMOU lies in estimating the number of latent factors. FMOU takes 8.13, 4.77 and 3.20 seconds for $\sigma_0^2 = 0.01^2, 0.05^2, 0.2^2$ to estimate the number of latent factors, d , respectively.

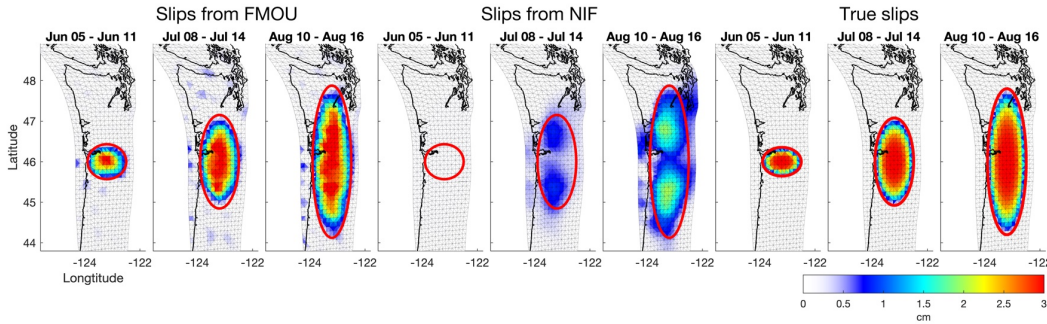


Figure 7: Seven-day averages of slips estimated by FMOU (left 3 panels) and NIF (middle 3 panels) in Experiment 5 when $\sigma_0^2 = 0.01^2 \text{ cm}^2$. The true slips (right 3 panels) propagate as a growing ellipse. The red boundary shows the front of the slip region.

contains observations from $\tilde{k} = 100$ GPS stations over $n = 88$ days in 2011 (Bartlow et al., 2011). Each observation represents the daily average geographical position recorded in three directions: East-West, North-South and Up-Down. We follow Bartlow et al. (2011) to use GPS measurements in the East-West and North-South directions, as the vertical displacement measurements contain little information for slip estimation. Figure 8(a) shows the cumulative displacements in the Cascadia region between June 3, 2011 to August 30, 2011, while the displacements in the East-West and North-South directions of six GPS stations are shown in Figure 8(b). As identified in DeMets et al. (2010), the observations encompass secular signals, such as annual and semiannual components, which are typically removed before the analysis (Bartlow et al., 2011). Details of preprocessing GPS measurements before modeling are provided in Section ?? in the supplement materials. Apart from the GPS measurements, we utilize determinations of tectonic tremor locations from the same region and period (Wech and Creager, 2008) as an independent assessment of the location of fault slip at a given time.

The Green's functions used here are built on a triangular mesh consisting of $k' = 1978$ triangular patches (Fukushima et al., 2005) located on a fault plane beneath the ground and they are calculated by assuming triangular dislocations in a homogeneous and elastic half-space (Thomas, 1993). Observations from 100 GPS stations in two directions yield

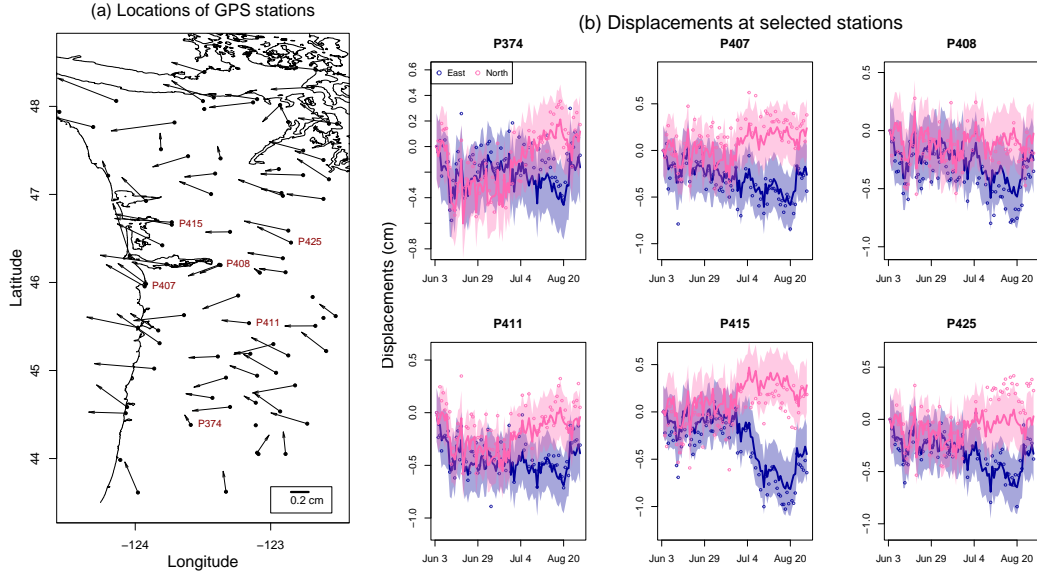


Figure 8: (a) The cumulative displacements from June 3, 2011 to August 30, 2011 in the Cascadia region are plotted by dark arrows with the unit of the measurements given in the inset. (b) The displacements by six GPS stations in East-West and North-South directions during the 2011 episodic tremor and slip event in centimeters (cm). The solid lines and corresponding shaded regions represent the predictive mean of the data and the 95% posterior credible intervals by FMOU, respectively.

a 200×1978 Green's function matrix \mathbf{G} . Furthermore, measurements are typically influenced by uncertainty in assigning the GPS-derived displacements in a North American Plate fixed reference frame, and local displacements of the GPS monuments. Thus it is common to include the frame motion or a time-dependent trend of each direction shared by each GPS station (Bartlow et al., 2011). Consequently, the augmented model can be written as $\mathbf{y}(t) = \mathbf{G}^{aug} \mathbf{z}_s^{aug}(t) + \epsilon(t)$, where $\mathbf{G}^{aug} = (\mathbf{G}, \mathbf{I}_{k \times 2})$ with $\mathbf{I}_{k \times 2} := (\mathbf{I}_2, \dots, \mathbf{I}_2)^T$, and $\mathbf{z}_s^{aug}(t) = [\mathbf{z}_s(t)^T, f_E(t), f_N(t)]^T$ with $f_E(t)$ and $f_N(t)$ being the frame motion in the East-West and North-South directions, respectively, for $t = 1, \dots, n$. The Gaussian noise vector follows $\epsilon(t) \sim N(0, \sigma_0^2 \mathbf{I}_k)$ with σ_0^2 being the observed variance. Following Bartlow et al. (2011), we estimate the magnitude of the fault slips projected onto a horizontal plane at 52 degrees clockwise from North along with fault direction (DeMets et al., 2010).

We compare three methods. For FMOU, we use the VM method in (22) for estimating the number of latent factors and the parameters are estimated by Algorithm 1. We use the posterior mean of slip $\hat{\mathbf{z}}_s(t)$ from (21) for estimation. Then the slip rates are calculated by

$$(30) \quad \hat{\mathbf{z}}_{s,rate}(t) = \hat{\mathbf{z}}_s(t+1) - \hat{\mathbf{z}}_s(t),$$

for $t = 1, \dots, n-1$. Following Bartlow et al. (2011), we truncate the negative slip rates to zero, as it is deemed unlikely that the fault would slip backward in the prevailing tectonic stress state. For comparison, we include the NIF model (Segall and Matthews, 1997) and the modified NIF model (Bartlow et al., 2011), which are summarized in Section S4.2 and Section S4.3 in the supplementary materials, respectively.

5.2. Results. To evaluate the model performance, we use the held-out tremor locations to validate the estimation, as tremor is well associated in both space and time with fault slip. The tremors are monitored continuously in the Cascadia zone (Wech and Creager, 2008; Wech,

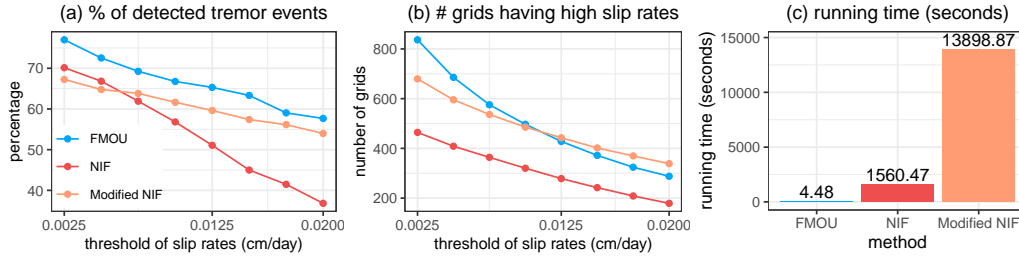


Figure 9: Model performance in 2011 Cascadia data. We compare three methods: FMOU (blue), NIF (red), and modified NIF (orange). (a) Proportion of identified tremor. (b) The number of grids containing large average slip rates. (c) Running time (seconds).

2010), available from the Pacific Northwest Seismic Network (PNSN) catalog. We consider two metrics: the proportion of tremors identified by large slip rates, and the total areas containing large slip rates for evaluating the true positive rate and positive rate, respectively.

Panels (a)-(b) in Figure 9 show the proportion of detected tremor events and the number of grids that contain high slip rates. The FMOU model detected the highest number of tremor events among all methods across all thresholds of the slip rates. A slip rate larger than 0.0125 cm/day is considered to be high. The FMOU model has a smaller number of spatial grids detected to have a high slip rate and it detects around 5% more tremors than the modified NIF model, shown in panel (b) of Figure 9. The NIF model has a substantially lower true positive rate compared to the modified NIF and FMOU, as it estimates slip rates to be negative or close to zero for more grids than the other two models. Because the noise in GPS measurement is relatively large compared to the slip-generated signal, a flexible model is preferred for capturing the heterogeneous slip changes. The FMOU model, with distinct correlation and variance parameters for each latent process, is more flexible than the NIF and modified NIF for modeling the slip propagation.

The computational time of the three methods is given in panel (c) in Figure 9. Notably, the computational time of the FMOU is more than 300 times and 3000 times faster than the NIF model and the modified NIF model, respectively. The most computationally intensive step for the FMOU is estimating the number of factors, which takes 3.56 seconds. After selecting the number of latent processes, estimating all parameters and slip rates requires only 0.92 seconds. This dramatic acceleration in computation enables the use of massive datasets from large GPS networks, and provides new opportunities to jointly estimate the hazards across larger regions, which could otherwise be prohibitive due to the large computational expense.

Figure 10 shows the seven-day average of the estimated slip rates of three periods by the FMOU, NIF and modified NIF models, where the solid dots represent the tremor epicenters. Estimation of slip rates of other periods is provided in Section S6 in supplementary materials. The estimates from FMOU align well with tremor dataset events, even though the GPS measurements and tremor datasets were collected independently from distinct sources. Compared to the modified NIF, the FMOU model provides better agreement between high-slip regions and tremor epicenters during August 10–16. In contrast, the modified NIF model detects a much larger area with relatively high slip rates, resulting in a higher false positive rate. Both FMOU and modified NIF reveal an area of high slip rates centered around 45°N and 123.5°W in early June, and another region with high slip rates centered around 47.5°N and 123°W in early August. However, the migration of the estimated high slip rates region is less apparent in the NIF model and its modified version. It's worth mentioning that the finding from the FMOU model is consistent with previous work by Bartlow et al. (2011), which illustrates the physical mechanism of the coincidence between tremor centers and the regions with high slip rates.

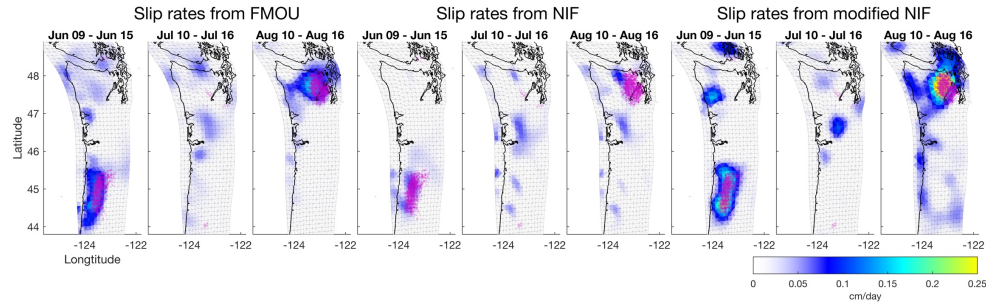


Figure 10: The seven-day averages of slip rates estimated by the FMOU, NIF and modified NIF are plotted in the left 3, middle and right 3 panels, respectively, for the Cascadia displacement data in 2011. The tremor epicenters are plotted as magenta dots.

6. Conclusion. In this paper, we proposed fast multivariate Ornstein-Uhlenbeck (FMOU) approach for estimating high-dimensional dynamical systems with noisy observations. We assumed a latent factor model with an orthogonal factor load matrix, where each latent process is modeled by an O-U process with distinct correlation and variance parameters estimated from the data. We derived a scalable EM algorithm in which each iteration contains closed-form expressions for parameter estimation and it does not require inverting large covariance matrix at each time in a Kalman filter. Extensive simulated studies and the real-world slip estimation example in the Cascadia region illustrate the high efficiency and scalability of the FMOU approach compared to other methods.

This study opens the door to various research problems in both methodology and applications. First, the O-U process is not mean-squared differentiable, so it may be of interest to extend the closed-form expressions for parameter estimation to differentiable Gaussian processes with Matérn covariance. Second, generalizing the fast algorithm to handle observations with irregular missing values is another interesting topic. Third, the FMOU implicitly induces a vector autoregressive model with a symmetric transition matrix in (26) for the mean of the observations. The high computational scalability and closed-form estimation of parameters make it appealing for applications such as scalable estimators for Granger causality from noisy data. For the application of slip estimation, the significantly faster approach by FMOU enables integrating geodetic data from large GPS networks, seismic data, and satellite interferograms for geological hazard quantification.

REFERENCES

- Aki, K. (1980). Quantitative seismology. *Theory and models.*, 1:932p.
- Anderson, K. R., Johanson, I. A., Patrick, M. R., Gu, M., Segall, P., Poland, M. P., Montgomery-Brown, E. K., and Miklius, A. (2019). Magma reservoir failure and the onset of caldera collapse at Kilauea volcano in 2018. *Science*, 366(6470).
- Bai, J. and Ng, S. (2002). Determining the number of factors in approximate factor models. *Econometrica*, 70(1):191–221.
- Bartlow, N. M., Miyazaki, S., Bradley, A. M., and Segall, P. (2011). Space-time correlation of slip and tremor during the 2009 cascadia slow slip event. *Geophysical Research Letters*, 38(18).
- Berkooz, G., Holmes, P., and Lumley, J. L. (1993). The proper orthogonal decomposition in the analysis of turbulent flows. *Annual review of fluid mechanics*, 25(1):539–575.
- Bock, Y., Agnew, D. C., Fang, P., Genrich, J. F., Hager, B. H., Herring, T. A., Hudnut, K. W., King, R. W., Larsen, S., Minster, J.-B., et al. (1993). Detection of crustal deformation from the landers earthquake sequence using continuous geodetic measurements. *Nature*, 361(6410):337–340.
- Bürgmann, R. (2018). The geophysics, geology and mechanics of slow fault slip. *Earth and Planetary Science Letters*, 495:112–134.

- Carslaw, H. S. (1906). *Introduction to the Mathematical Theory of the Conduction of Heat in Solids*. Macmillan and Company, limited.
- Cerbino, R. and Trappe, V. (2008). Differential dynamic microscopy: probing wave vector dependent dynamics with a microscope. *Phys. Rev. Lett.*, 100(18):188102.
- DeMets, C., Gordon, R. G., and Argus, D. F. (2010). Geologically current plate motions. *Geophysical journal international*, 181(1):1–80.
- Fukushima, Y., Cayol, V., and Durand, P. (2005). Finding realistic dike models from interferometric synthetic aperture radar data: The february 2000 eruption at piton de la fournaise. *Journal of Geophysical Research: Solid Earth*, 110(B3).
- Gardiner, C. W. (1985). Handbook of stochastic methods for physics, chemistry and the natural sciences. *Springer series in synergetics*.
- Gelfand, A. E., Schmidt, A. M., Banerjee, S., and Sirmans, C. (2004). Nonstationary multivariate process modeling through spatially varying coregionalization. *Test*, 13(2):263–312.
- Gomberg, J., 2007, C., and Group, B. W. (2010). Slow-slip phenomena in cascadia from 2007 and beyond: A review. *Bulletin*, 122(7-8):963–978.
- Gu, M., He, Y., Liu, X., and Luo, Y. (2024a). Ab initio uncertainty quantification in scattering analysis of microscopy. *Physical Review E*, 110(3):034601.
- Gu, M., Lin, Y., Lee, V. C., and Qiu, D. Y. (2024b). Probabilistic forecast of nonlinear dynamical systems with uncertainty quantification. *Physica D: Nonlinear Phenomena*, 457:133938.
- Gu, M. and Shen, W. (2020). Generalized probabilistic principal component analysis of correlated data. *Journal of Machine Learning Research*, 21(13).
- Hotelling, H. (1933). Analysis of a complex of statistical variables into principal components. *Journal of educational psychology*, 24(6):417.
- Kalman, R. E. (1960). A new approach to linear filtering and prediction problems. *Journal of basic Engineering*, 82(1):35–45.
- Lam, C. and Yao, Q. (2012). Factor modeling for high-dimensional time series: inference for the number of factors. *The Annals of Statistics*, 40(2):694–726.
- Lam, C., Yao, Q., and Bathia, N. (2011). Estimation of latent factors for high-dimensional time series. *Biometrika*, 98(4):901–918.
- Lorenz, E. N. (1996). Predictability: A problem partly solved. In *Proc. Seminar on predictability*, volume 1.
- Lu, H. and Tartakovsky, D. M. (2020). Prediction accuracy of dynamic mode decomposition. *SIAM Journal on Scientific Computing*, 42(3):A1639–A1662.
- Meucci, A. (2009). Review of statistical arbitrage, cointegration, and multivariate Ornstein-Uhlenbeck. *Cointegration, and Multivariate Ornstein-Uhlenbeck (May 14, 2009)*.
- Rauch, H. E., Tung, F., and Striebel, C. T. (1965). Maximum likelihood estimates of linear dynamic systems. *AIAA journal*, 3(8):1445–1450.
- Sabass, B., Gardel, M. L., Waterman, C. M., and Schwarz, U. S. (2008). High resolution traction force microscopy based on experimental and computational advances. *Biophysical journal*, 94(1):207–220.
- Schmid, P. J. (2010). Dynamic mode decomposition of numerical and experimental data. *Journal of fluid mechanics*, 656:5–28.
- Segall, P. and Matthews, M. (1997). Time dependent inversion of geodetic data. *Journal of Geophysical Research: Solid Earth*, 102(B10):22391–22409.
- Soetaert, K. E., Petzoldt, T., and Setzer, R. W. (2010). Solving differential equations in R: package deSolve. *Journal of statistical software*, 33(9).
- Thomas, A. L. (1993). Polu3d: A three-dimensional, polygonal element, displacement discontinuity boundary element computer program with applications to fractures, faults, and cavities in the earth’s crust. *Master Thesis at Stanford University*.
- Tipping, M. E. and Bishop, C. M. (1999). Probabilistic principal component analysis. *Journal of the Royal Statistical Society: Series B (Statistical Methodology)*, 61(3):611–622.
- Tu, J. H., Rowley, C. W., Luchtenburg, D. M., Brunton, S. L., and Kutz, J. N. (2014). On dynamic mode decomposition: Theory and applications. *Journal of Computational Dynamics*, 1(2):391–421.
- Wech, A. G. (2010). Interactive tremor monitoring. *Seismological Research Letters*, 81(4):664–669.
- Wech, A. G. and Creager, K. C. (2008). Automated detection and location of Cascadia tremor. *Geophysical Research Letters*, 35(20).
- Wen, Z. and Yin, W. (2013). A feasible method for optimization with orthogonality constraints. *Mathematical Programming*, 142(1-2):397–434.
- Yabuki, T. and Matsu’Ura, M. (1992). Geodetic data inversion using a bayesian information criterion for spatial distribution of fault slip. *Geophysical Journal International*, 109(2):363–375.